

pubs.acs.org/joc Article

# Mechanistic Insight into Phenol Dearomatization by Hypervalent Iodine: Direct Detection of a Phenoxenium Cation

Antoine Juneau, Iannick Lepage, Sami G. Sabbah, Arthur H. Winter, and Mathieu Frenette\*



Cite This: J. Org. Chem. 2022, 87, 14274–14283



**ACCESS** I

III Metrics & More

Article Recommendations

SI Supporting Information

ABSTRACT: Phenol dearomatization is one of several oxidation reactions enabled by hypervalent iodine reagents. However, the presence of a proposed free phenoxenium intermediate in phenol dearomatization is a matter of debate in the literature. Here, we report the unambiguous detection of a free phenoxenium intermediate in the reaction of an electron-rich phenol, 2,4,6-trimethoxyphenol, and (diacetoxyiodo)benzene using UV—vis and resonance Raman spectroscopies. In contrast, we predominantly detect single electron oxidation products of less electron-rich phenols or alkoxy-substituted aromatics in their reaction with (diacetoxyiodo)benzene using UV—vis and electron paramagnetic resonance (EPR) spectroscopies. We conclude that the often-postulated free phenoxenium intermediate, while possible with highly stabilizing substituents, is unlikely to be a general mechanistic pathway in the reaction of typical phenols with hypervalent iodine reagents. The polar solvent 1,1,1,3,3,3-hexafluoroisopropanol (HFIP) or

the use of more strongly oxidizing hypervalent iodine reagents, such as [bis(trifluoroacetoxy)iodo]benzene (PIFA) or [hydroxy(tosyloxy)iodo]benzene (HTIB), can help reduce the formation of radical byproducts and favors the formation of phenoxenium intermediates.

## **■ INTRODUCTION**

Hypervalent iodine (HVI) compounds are versatile oxidizing agents that appear in a growing number of reactions such as Hofmann and Beckmann rearrangements, cross-coupling of phenols, as well as phenol and aniline dearomatizations. <sup>1,2</sup> HVI compounds also find use in the push for green alternatives to commonly employed metal oxidants—they are generally of lower toxicity, easier to handle, and more environmentally friendly than complexes containing mercury(II), thallium(III), or lead(IV).3 A ubiquitous hypervalent iodine reagent is (diacetoxyiodo)benzene, PhI(OAc)2, also called DIB or phenyliodine(III) diacetate (PIDA). As with other HVI compounds, the thermodynamic driving force behind this strong, yet selective, oxidizing agent is the formation of stable products following its two-electron oxidation reaction: iodobenzene and acetate. In the specific example of phenol dearomatization using PIDA (Scheme 1a), the phenol becomes an electrophile capable of accepting a nucleophilic attack in the ortho or para position. The selectivity of hypervalent iodine reactions is related to its mechanism of oxidation; however, its mechanism remains unclear and is a matter of active scientific interest. Classically, phenol dearomatization reactions are said to proceed via a phenoxenium (1, also called aryloxenium or phenyl oxenium intermediate that bears a formal positive charge on its oxygen). The phenoxenium cation can readily be attacked by a nucleophile to yield the corresponding dearomatized product

(3, Scheme 1a). The presence of a true phenoxenium intermediate in these reactions is, however, still debated.

Several mechanistic studies show contradicting evidence for this reaction intermediate and no direct observation of a phenoxenium formed during HVI reactions has been reported. It was observed that stereocontrol in products formation can be induced by a chiral HVI reagent, hinting at an associative mechanism in which the nucleophile attacks a phenoxy- $\lambda^3$ iodane intermediate 2.4 Hammett analysis and DFT studies on substituted 4-phenylphenols oxidation support the formation of a proper phenylphenoxenium intermediate, which would be formed by heterolysis of a 4-phenylphenoxy-λ<sup>3</sup>-iodane.<sup>5,6</sup> A recent study by Kraszewski, et al. for the dearomatizing hydroxylation of 2,4-di-<sup>t</sup>Bu-phenol 4 (Scheme 1b) confirmed, by electron paramagnetic resonance (EPR) spectroscopy, the presence of phenoxyl radical 5. In their proposed mechanism, no phenoxenium intermediate was needed. The reaction instead proceeds via radical chain propagation due to an iodanyl radical 6. The phenoxyl radical could realistically be formed by homolysis of a phenoxy- $\lambda^3$ -iodane or by single

Received: July 25, 2022 Published: October 10, 2022





Scheme 1. Possible Pathways for Phenol Oxidation Using Hypervalent Iodine

"(a) Heterolytic dissociation of a phenoxy- $\lambda^3$ -iodane intermediate 2 into a phenoxenium cation 1 results in the formation of the dearomatized product 3 according to the "classic" mechanism. An associative mechanism is also possible, allowing enantiomeric control if a chiral hypervalent iodine is used. (b) Radical chain mechanism proposed by Kraszewski et al. during the oxidation of 2,4-di-Bu-phenol. (c) Plausible isomerization and homolytic dissociation of an intermediate 7 during the oxidation of p-cresol could yield the corresponding phenoxyl radical 9, as considered by density functional theory (DFT) by Ganji and Ariafard. (d) Oxidation of 2,4,6-trimethoxyphenol leads to the direct detection of the phenoxenium intermediate TMP-O+, as reported herein.

electron transfer (SET) from the starting phenol to PIDA, followed by deprotonation. The homolysis pathway of phenoxy- $\lambda^3$ -iodane 7 has been considered before by DFT for p-cresol, and although it was found to be more energetic than the heterolytic dissociation, it remains an outcome worth noting for the formation of phenoxyl radicals like 9 (Scheme 1c).

Contradicting evidence points to the idea that all mechanisms are likely active and competing with each other. One route may be kinetically favored depending on the starting phenol's substituents and electron-donating capabilities as well as reaction conditions. For example, *p*-methoxy substituents stabilize the cation and favor a dissociative route, evidenced by the loss of stereocontrol when using chiral HVI. It has also been shown that a fluorinated solvent such as 1,1,1,3,3,3-hexafluoroisopropanol (HFIP) is required to achieve high yields, a process which has been attributed in part to the specific hydrogen bonding between HFIP and an acetate moiety of PIDA that makes it strongly oxidizing. 11

This ionizing solvent is also known to stabilize cationic intermediates like phenoxenium, decreasing enantiomeric control by helping heterolytic dissociation. However, despite being the most proposed intermediate, the detection of a phenoxenium in HVI-based reactions has never been achieved.

Herein, we describe the first direct identification of a free phenoxenium intermediate by UV—vis and resonance Raman spectroscopies during phenol dearomatization reactions using hypervalent iodine. This was made possible using PIDA as the oxidizing agent and the electron-rich 2,4,6-trimethoxyphenol (TMP-OH) as the substrate (Figure 1d). Methoxy groups strongly stabilize the corresponding phenoxenium cation TMP-O<sup>+</sup> due to the delocalization of the positive charge on the *ortho* and *para* positions, which made clear detection possible. Similar reactions using methoxy-substituted phenols have been used for useful synthesis in the context of HVI reactions. However, phenoxenium cations are not readily observed during HVI oxidation reactions when using less electron-rich phenols (vide infra), while the presence of a phenoxyl radical intermediate could be detected by UV—vis

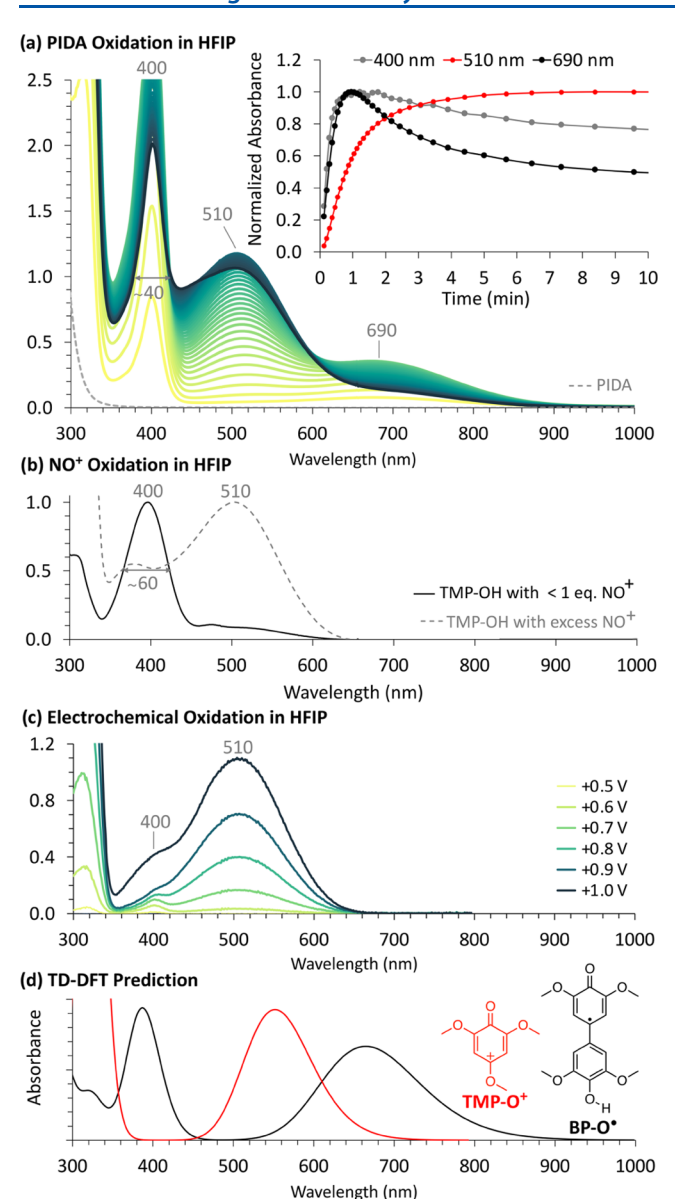


Figure 1. UV—vis spectra of TMP-OH under various oxidizing conditions. (a) Absorption changes during the reaction between PIDA (1.31 mM) and TMP-OH (1.26 mM) in HFIP at 10 °C for 30 min. The dashed gray line shows the absorption of PIDA before the addition of TMP-OH. The inset shows the kinetic traces for the absorption at 400, 510, and 690 nm for the first 10 min. (b) TMP-OH in HFIP oxidized by <1 equiv (black line) or an excess (gray dashed line) of NO<sup>+</sup> salt, both normalized to their  $\lambda_{\rm max}$ . (c) Spectra obtained during the electrochemical oxidation of TMP-OH (9.84 mM) in HFIP with electrolytes and at room temperature. The working electrode is Au, and the pseudo-reference electrode is Ag/Ag<sup>+</sup>. (d) Comparison with the time-dependent density functional theory (TD-DFT)-predicted absorption spectra for TMP-O<sup>+</sup> and the dimeric byproduct BP-O<sup>+</sup>.

and EPR. Using spectroscopic and DFT methods, we explore possible mechanistic outcomes for the oxidation of a trimethoxy-substituted phenol with HVI. The need for such an electron-rich phenol to observe a free phenoxenium in these reactions suggests that this intermediate is specific to substrates that strongly stabilize the phenoxenium ion and is not ubiquitous to all phenol dearomatization reactions.

#### RESULTS AND DISCUSSION

Since phenoxyl radicals and phenoxenium cations generally show strong UV-vis absorption signals, we first studied the kinetics of phenol oxidation using this technique. Mixing PIDA and TMP-OH in the fluorinated solvent HFIP led to the formation and decay of reaction intermediates with absorption maxima at 400, 510, and 690 nm (Figure 1a). All three peaks in the visible region could be quenched by the addition of water (Figure S4) and were stabilized by lowering the reaction temperature, confirming their reactive nature. In the absence of water, the absorption decay of the intermediates was offset by the formation of products with  $\lambda_{\text{max}} \approx 500$  nm, which explains why the 510 nm intermediate appears to be stable in the kinetic trace. Reacting TMP-OH with PIDA gave an absorption peak at 510 nm that was unequivocally assigned to the phenoxenium cation intermediate TMP-O+ by resonance Raman (vide infra). Substituting PIDA with HVI of higher oxidizing power, namely, [bis(trifluoroacetoxy)iodo]benzene (PIFA) and hydroxy(tosyloxy)iodobenzene (HTIB), immediately led to TMP-O<sup>+</sup> (see Figure S12). No other intermediate was observed by UV-vis spectroscopy in these cases, indicating that oxidation is a lot faster with PIFA and HTIB. A similar absorption at 510 nm was also generated by reacting TMP-OH with an excess of strongly oxidizing nitrosonium (NO+) salts (Figure 1b) and by using electrochemical oxidation (Figure 1c). TD-DFT calculations using B3LYP/Def2TZVP,SMD(HFIP) predict a similar absorption maximum for TMP-O+ (Figure 1d). Because the 510 nm peak is observed regardless of the oxidation method, we conclude it is not an iodine-specific species and is consistent with the formation of free TMP-O+. Titration experiments, this time using PIFA, a more reactive oxidant HVI, allowed us to estimate the molar absorption coefficient for TMP-O $^+$  as 2.2  $\times$  $10^3 \text{ M}^{-1} \text{ cm}^{-1}$  at 510 nm (see Figure S6).

Phenoxyl radicals are also expected intermediates during phenol oxidation reactions. In addition to the peak at 510 nm, which we assigned to TMP-O<sup>+</sup>, the reaction of TMP-OH with PIDA in HFIP shows absorptions centered at 400 and 690 nm (Figure 1a). We initially considered the possibility that the 400 nm peak could be attributed to the phenoxyl radical TMP-O<sup>+</sup>. A similar peak at 400 nm (Figure 1b) was observed during the oxidation of TMP-OH by less than 1 equiv of NO<sup>+</sup>, which is consistent with the formation of a one-electron oxidation product like TMP-O<sup>+</sup>. Upon closer examination, however, the full width at half-maximum (FWHM) for the 400 nm peak during NO<sup>+</sup> oxidation is significantly larger (~60 nm) than the peak formed during PIDA oxidation (~40 nm), suggesting that these are distinct species.

We attribute the absorption peak at 400 nm in the NO<sup>+</sup> oxidation of TMP-OH to TMP-O<sup>•</sup> since EPR data and simulation (Figure 3a) confirm this assignment (see the EPR Detection of a Radical Intermediate section for more details). Importantly, the absorption peak at 690 nm seen during PIDA oxidation of TMP-OH (Figure 1a) is missing in the NO<sup>+</sup> oxidation experiments (Figure 1b). With the help of EPR measurements (Figure 3b) and TD-DFT absorption predictions (Figure 1d), we tentatively assign the two peaks at 400 and 690 nm for the PIDA oxidation of TMP-OH to a biphenyl intermediate corresponding to the hydrocoerulignone phenoxyl radical (BP-O<sup>•</sup>, Figure 1d). We postulate the initial carboncarbon bond between the two phenols is formed by the attack of TMP-OH to TMP-O<sup>+</sup>. The exact mechanism by which two

methoxy groups leave is not immediately clear to us, but this type of reaction has been proposed in the literature. <sup>16</sup>

During the oxidation of TMP-OH by NO+, TMP-O is formed by a stoichiometric one-electron oxidation followed by proton loss. When using an excess of NO+, the peak at 400 nm is converted to 510 nm due to the subsequent one-electron oxidation of TMP-O into TMP-O. The same TMP-O cation absorbing at 510 nm is also observed during the electrochemical oxidation of TMP-OH. In this case, potentials of ca. +0.7 V vs Ag/Ag<sup>+</sup> were required. The irreversibility of this oxidation peak observed in the cyclic voltammogram (CV) (see Figure S22) suggests a three-step mechanism that undergoes electron transfer, chemical reaction, and electron transfer (ECE). ECE mechanisms are known for the 2e<sup>-</sup>/1H<sup>+</sup> oxidation of phenol into phenoxenium as seen in another palkoxyphenol, the  $\alpha$ -tocopherol. 12 It was shown that the first and second electron transfer occurs at almost identical potentials, indicating that the phenoxyl radical is rapidly converted into the phenoxenium. This experiment rationalizes why the phenoxyl radical is difficult to obtain at high concentrations by electrochemical methods.

Phenoxenium Detection via Resonance Raman. We identified by TD-DFT that the 510 nm transition of TMP-O<sup>+</sup> corresponds to the HOMO  $\rightarrow$  LUMO transition ( $S_0 \rightarrow S_1$ ). It coincides well with the 532 nm Raman wavelength available to us and was therefore ideal for the selective amplification of the phenoxenium's Raman signal due to the resonance effect. The DFT-predicted pre-resonance Raman spectrum for TMP-O<sup>+</sup> (Figure 2a) nicely matches the experimental Raman spectrum of TMP-OH reacting with NO<sup>+</sup> in CH<sub>3</sub>CN (Figure 2b).

UV-vis monitoring of its peak at 510 nm shows that it is long-lived at room temperature when oxidized by NO<sup>+</sup> (see

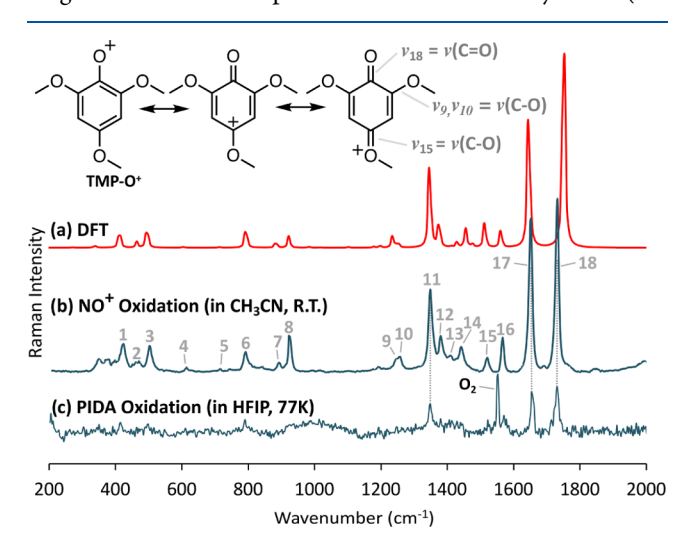


**Figure 2.** Resonance Raman spectra using 532 nm excitation confirming the conversion of TMP-OH into TMP-O $^+$ . (a) DFT-predicted spectra of TMP-O $^+$  using B3LYP/Def2TZVP,SMD(HFIP) with pre-resonance effect. (b) Experimental spectra obtained by oxidizing TMP-OH (6.8 mM) with NO $^+$ SbF $_6^-$  (26.7 mM) in anhydrous CH $_3$ CN and at room temperature. (c) Experimental spectra of a freeze-quenched mixture of TMP-OH (412 mM) and PIDA (459 mM) recorded at 78 K ( $^-$ 195 °C). The contributions from the solvent and the products were subtracted from spectra (b) to isolate the signal of TMP-O $^+$  (see Figure S14). The peak at 1552 cm $^{-1}$  in (c) comes from ambient O $_2$  dissolved in liquid nitrogen. Three resonance forms contributing to the stability of TMP-O $^+$  are shown at the top.

Figure S5b). In the case of PIDA oxidation, however, the reaction mixture was unstable and had to be freeze-quenched. Figure 2c shows the resonance Raman spectrum of this mixture obtained at 77 K (-196 °C).

Despite the low signal-to-noise ratio, clear detection of TMP-O<sup>+</sup> is deduced from the presence of the peaks at 1347 cm<sup>-1</sup> ( $\nu_{11}$ ), 1649 cm<sup>-1</sup> ( $\nu_{17}$ ) and 1731 cm<sup>-1</sup> ( $\nu_{18}$ ). These vibrations correspond to an aromatic C–C stretch, a symmetric ring C=C stretch, and a C=O stretch, respectively. Selective amplification of the bands  $\nu_{17}$  and  $\nu_{18}$  through a resonance mechanism is also consistent with the geometry of the S<sub>1</sub> state of phenoxeniums which are known to have elongated C=C and C=O bonds<sup>17</sup> (see Figure S19).

Overall, we could identify 18 peaks for TMP-O<sup>+</sup> and found that both the vibrational frequencies and intensities of these peaks are in very good agreement with predictions as long as S<sub>1</sub> resonance enhancement effects are considered (Figure S18). All of the peaks identified for TMP-O<sup>+</sup> in Figure 1b were quenched by the addition of 0.5% v/v of water, leading to the formation of 2,6-dimethoxybenzoquinone (compound 12, detected by gas chromatography—mass spectrometry (GC—MS), see Figure S13). This benzoquinone is a known product for the oxidation of TMP-OH, including by HVI compounds.<sup>19</sup> The Raman laser sources available to us could not reach the 400 and 690 nm peaks, suspected to be the neutral radical species. Thus, to assign the remaining intermediate, we resorted to EPR spectroscopy.

**EPR Detection of a Radical Intermediate.** As shown previously in the UV-vis spectra in Figure 1b, mixing TMP-OH with a stoichiometric amount of NO<sup>+</sup> salt led to the selective formation of TMP-O• with a peak of  $\lambda_{max} = 400$  and FWHW =  $\sim 60$  nm. We used X-band EPR spectroscopy to unambiguously assign this radical. Figure 3a shows the resulting spectra when recorded at 283 K (10 °C) in HFIP.

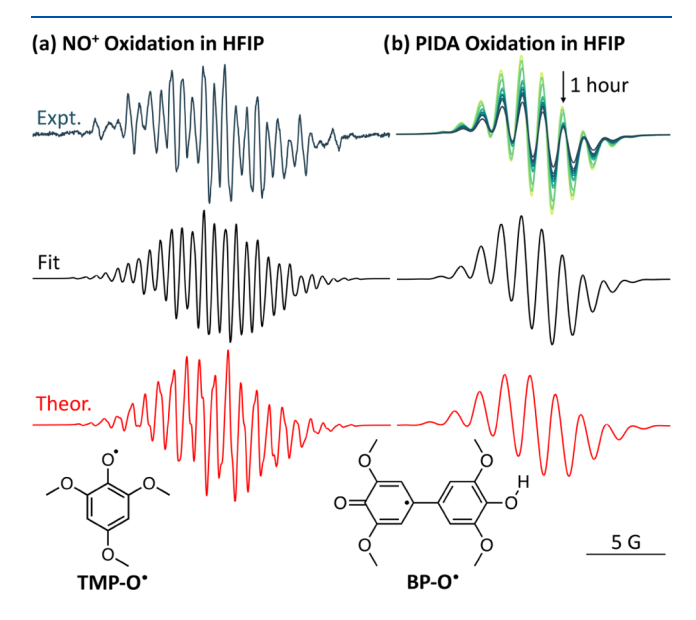
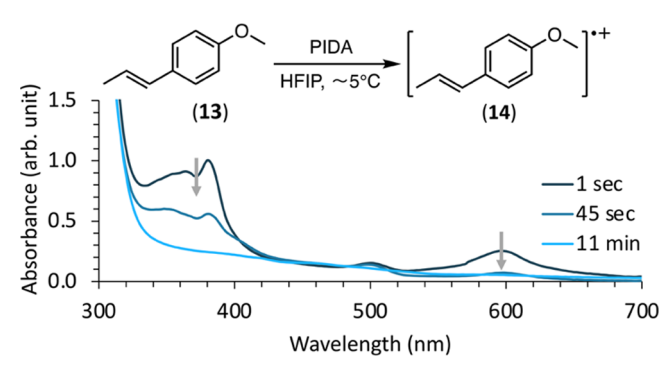


Figure 3. (a) EPR spectra for the reaction of TMP-OH (16.3 mM) with NO $^+$ BF $_4^-$  (16.6 mM). (b) EPR spectra for the reaction of TMP-OH (1.66 mM) with PIDA (1.67 mM). Both were obtained at 10  $^\circ$ C in HFIP. The experimental spectra are shown at the top, the best simulation fittings are shown in middle, and the DFT-predicted spectra are shown at the bottom. Obtained with B3LYP/EPR-III,SMD(HFIP) and simulated with the garlic module of EasySpin  $5.^{20}$ 

The simulated fit for the phenoxyl radical **TMP-O** is in good agreement with the experimental spectrum, and so is the DFT-predicted spectrum. This radical's EPR has been reported elsewhere, and the *g*-value of 2.0044 we measured is close to theirs (g = 2.0050 in benzene). The hyperfine coupling constants are also consistent and can be found in Table S2. As a precaution, we also considered the possibility of another  $1e^-$  oxidation product: the 2,4,6-trimethoxyphenol radical cation  $[\mathbf{TMP-OH}]^{\bullet+}$ . The simulated fit and predicted spectra for this compound were in poor agreement with our experimental signal due to the strong hyperfine coupling of the extra proton, and this possibility was ruled out.

Dimeric Byproduct Formation. When using PIDA as the oxidizing agent instead of NO+, an EPR signal different from TMP-O was obtained (Figure 3b). The g-value of 2.0046 indicates low spin-orbit coupling (i.e., not an iodanyl compound such as 10). This was also confirmed by substituting PIDA with its fluorinated version, PIFA, or by Dess-Martin periodinane, which led to the same EPR signal (albeit much less intense) in either case (Figures S24 and S25). Overall, DFT and TD-DFT predictions for the EPR and the UV-vis spectra of the dimeric product BP-O are in good agreement with experiments; BP-O would explain both the 400 and the 690 nm peaks observed during PIDA oxidation of TMP-OH. Titration experiments suggest that this dimer is formed when there is concurrent presence of both TMP-O+ and TMP-OH (see Figures S6 and S7). When the oxidation of TMP-OH into TMP-O+ is completed rapidly, and no excess phenol is available to attack the phenoxenium intermediate, no signal is detected at 690 nm. The peak at 690 nm was also absent in the case for electrochemical and NO+ oxidation, which we attribute to the rapid oxidation of TMP-OH at the electrode. When PIDA was used, the slow and selective 2e<sup>-</sup>/ H<sup>+</sup> loss of TMP-OH to yield TMP-O<sup>+</sup> led to a mixture of the oxidized and reduced state, therefore forming the dimer. Our attempts to isolate or detect the corresponding diphenoquinone product were however not successful, which brings doubt to this assignment. If it is indeed attributed to BP-O, we believe that it may only be found as a minor byproduct and that its large contribution in the UV-vis spectrum of Figure 1a would be due to its large extinction coefficient.

Possibility of a SET Mechanism. It has long been reported that electron-rich  $\pi$  systems such as methoxy aryls can donate an electron to PIFA through SET. 3,22,23 Similarly, transanethole (13) has been shown to dimerize when reacted with PIDA and the mechanism is said to proceed via the formation of a radical cation.<sup>24</sup> Upon mixing of trans-anethole with PIDA in HFIP, we observed the characteristic signal of its radical cation form (14) at  $\lambda_{\text{max}}$  of 390 and 600 nm (Figure 4).<sup>25</sup> This is another clear demonstration of a SET pathway for methoxycontaining aromatics since trans-anethole cannot bind to PIDA via ligand exchange as do phenols. With the clear observation of a SET mechanism in the reaction between trans-anethol and PIDA, we hypothesized that SET between PIDA and TMP-OH would be a likely mechanistic outcome in this reaction. If formed, [TMP-OH] o+ could rapidly lose a proton to yield TMP-O, and subsequent one-electron oxidation would generate the TMP-O+ we detected. As previously shown, the UV-vis and EPR experiments, however, do not indicate the presence of TMP-O nor [TMP-OH] +. These results indirectly support that TMP-O+ is formed from intermediate 11, as opposed to a stepwise 2e<sup>-</sup> SET oxidation process.



**Figure 4.** Oxidation of *trans*-anethole (8.6 mM) by PIDA (10.4 mM) in HFIP led to the direct UV—vis detection of the radical cation of trans-anethole with its characteristic absorption peaks at 380 and 600 nm.  $^{2.5}$ 

## Energy Profiles for Competing Mechanisms via DFT.

To bring further evidence in the mechanism for the formation of TMP-O+, we evaluated the possible outcomes using DFT. In the first considered mechanism, the reaction is initiated by a SET from TMP-OH to PIDA (Figure 5, SET pathway). This would generate the radical anion [PIDA] •- and the radical cation [TMP-OH] •+. The pKa values of phenol radical cations are low, and this intermediate would rapidly lose its proton. This scheme would be closer to a proton-coupled electron transfer (PCET) mechanism where the proton of the phenol is transferred to the acetate group of PIDA. DFT also confirmed this because our attempt to optimize [TMP-OH] + at the proximity of [PIDA] - reveals a barrierless H<sup>+</sup> transfer. To estimate an upper barrier to the SET step, we calculated the energy of the fully separated [TMP-OH]\* and [PIDA]\*-. This approximation will likely overestimate the energy barrier for the SET step. Once TMP-O is formed, it could transfer an electron to the iodanyl radical  $(10)^{26}$  to yield TMP-O<sup>+</sup> and the stable products iodobenzene and acetate. TMP-O\* could theoretically react with another molecule of PIDA via SET to yield TMP-O+ and [PIDA] - (Figure 5, dashed red line); however, this path is less thermodynamically favorable. The second pathway, shown on the right-hand side of Figure 5, corresponds to the dissociative route that is most often proposed to explain phenoxenium generation. First, isomerization of PIDA from the transition state TS1 opens up the lateral position, as previously reported by Ganji and Ariafard.8 This structure is highly reactive toward ligand exchange and phenol can easily bind to form the I-O bond while releasing acetic acid. As mentioned previously, the resulting phenoxy- $\lambda^3$ iodane 11 may then follow two paths of its own: heterolytic or homolytic dissociation. We calculated an activation free energy  $(\Delta G^{\ddagger})$  of 17.6 kcal mol<sup>-1</sup> for the heterolytic dissociation, which leads directly to TMP-O+. The formation of TMP-O• via homolysis of the same intermediate 11 is found to be less favorable, with an activation free energy of  $\sim 21.0$  kcal mol<sup>-1</sup>. This value was approximated by calculating the minimum energy crossing point (MECP) between the singlet and triplet surface, similar to Ganji and Ariafard.8 Inspection of the orbitals confirms that the two unpaired electrons of the triplet state are indeed disjoint: one is on the phenoxy moiety and the other on the iodanyl (Figure S27). Considering our DFT calculations and the kinetic trace shown in Figure 1a, it appears that the oxidation of TMP-OH occurs in a dissociative manner. This is consistent with the reported synthesis of other p-methoxyphenols by various HVI compounds, and with our

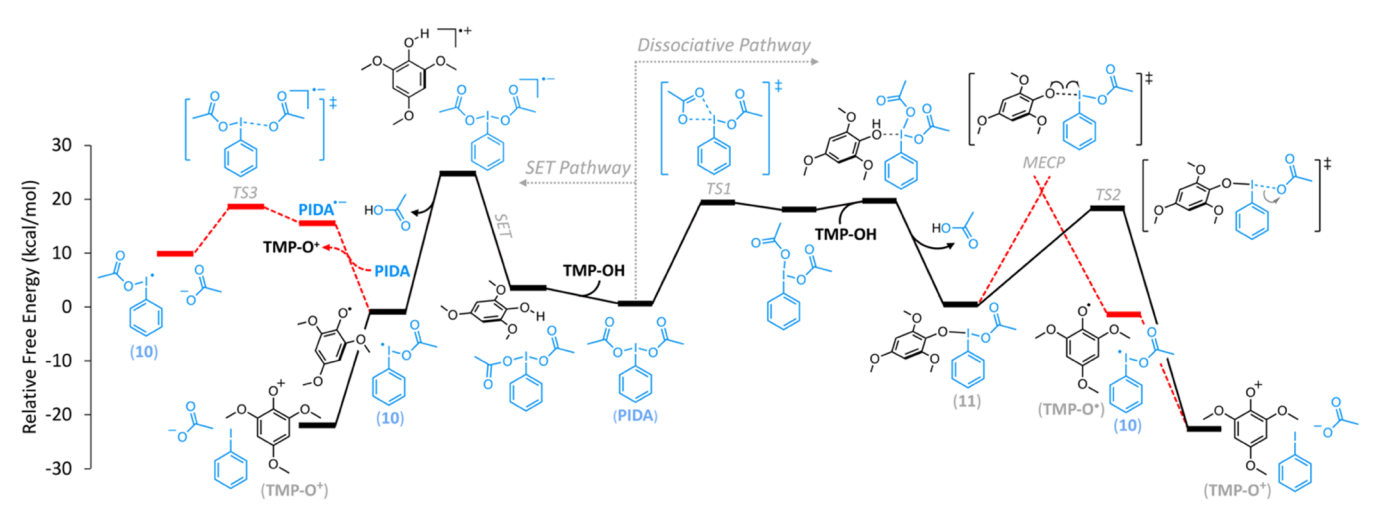


Figure 5. Calculated free energy profile comparing possible pathways to generate  $TMP-O^+$  from hypervalent iodine oxidation. (Left) Single electron transfer (SET) pathway and (right) dissociative mechanism, both calculated with M06-2X/Def2TZVP using SMD(HFIP). The most energetically favorable route is the heterolytic dissociation of a  $TMP-O-\lambda^3$ -iodane adduct (11) into  $TMP-O^+$  (TS2). Homolytic dissociation of the same adduct (11) into  $TMP-O^+$  is less favorable, and so is a SET mechanism.

detection of free TMP-O<sup>+</sup>. At this point, however, we cannot rule out a SET followed by proton loss (or proton-coupled electron transfer) to form TMP-O<sup>+</sup> and iodanyl radical 10 with rapid reoxidation of TMP-O<sup>+</sup> by 10 to TMP-O<sup>+</sup>.

Importance of HFIP. The solvent HFIP has seen increasing versatility in recent years for many synthetic reactions.  $^{11,27}$  To achieve high yields in phenol dearomatization that are said to proceed via phenoxenium, HFIP is often required in at least a small proportion, mixed with other solvents like CH<sub>3</sub>CN or CH<sub>2</sub>Cl<sub>2</sub>. 3,28 When working with CH3CN instead of HFIP in the oxidation of TMP-OH by PIDA, we could not detect any phenoxenium intermediate by UV-vis. A mixture of 50/50 HFIP:CH<sub>3</sub>CN led to some BP- $\boldsymbol{O}^{\bullet}$  and  $TMP\text{-}\boldsymbol{O}^{\scriptscriptstyle{+}}$  associated absorption signals but not as strong as with pure HFIP (see Figure S3). There are likely multiple important phenomena that can explain this observation. First, HFIP is a polar solvent with low nucleophilicity that can help stabilize phenoxenium intermediate but cannot attack the cationic position. It was also demonstrated by NMR that HFIP increases the oxidation power of PIDA by hydrogen bonding with the acetate moiety. 11 We found that HFIP was not required to obtain TMP-O+ if triflic acid was added. With a solvent mixture of 0.5% v/v triflic acid in CH<sub>3</sub>CN, oxidation of TMP-OH rapidly led to TMP-O+, without any detectable UV-vis signal from the byproduct BP-O. The rapid formation of TMP-O+ is likely associated with the in situ formation of iodine triflate,<sup>29</sup> increasing its oxidative power and bypassing the formation of BP-O for the kinetic reasons described earlier. The phenoxenium that was formed also showed no sign of degradation over 30 min in the solvent mixture of 0.5% v/v triflic acid in CH<sub>3</sub>CN (Figure S5c). The enhanced stability of TMP-O<sup>+</sup> in the presence of strong acid is likely due to the protonation of traces of water or other nucleophilic impurities and the increased oxidation potential of PIDA.

**Different Behavior in Other Phenols.** To see if the mechanism could be generalized to other phenols, we performed a similar spectroscopic investigation of the oxidation of the vitamin-E analogue 2,2,5,7,8-pentamethyl-6-chromanol (PMHC-OH). This substrate is biologically relevant, and its oxidation products has therefore been amply

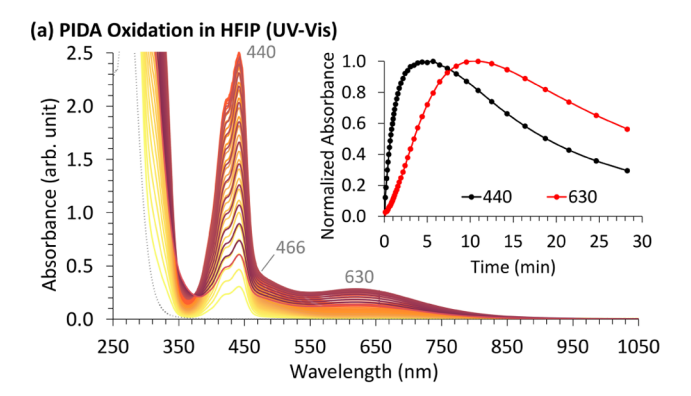
studied, contrary to TMP-OH. UV—vis measurements show that oxidation of PMHC-OH by PIDA led to the rapid growth of the phenoxyl radical (PMHC-O\*) at 440 nm. It is redshifted by 16 nm from the reported value in chlorobenzene but is recognizable by its higher-frequency shoulder around 424 nm. PMHC-O\* is also directly confirmed by EPR in the same reaction mixture (Figure 6d). Concerning the phenoxenium cation PMHC-O\*, it has already been detected by others during the oxidation of PMHC-OH by NO\* in CH<sub>3</sub>CN. Using low-temperature FTIR, they obtained its vibrational spectra. Similarly, we herein report the Raman signal of PMHC-O\* generated using NO\* in acetonitrile and frozen at 77 K—the measured resonance Raman decently matches the DFT prediction (Figure 6c).

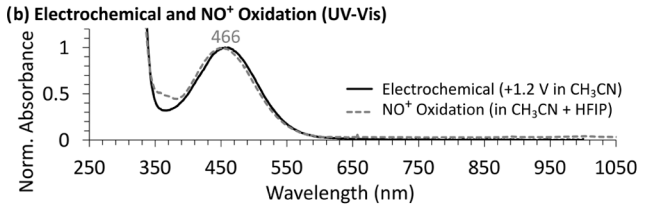
UV—vis experiments show that this bright red intermediate features a single and broad absorption peak in the visible range with  $\lambda_{\rm max}$  = 466 nm, somewhat shifted from the reported value of 452 nm. <sup>32</sup>

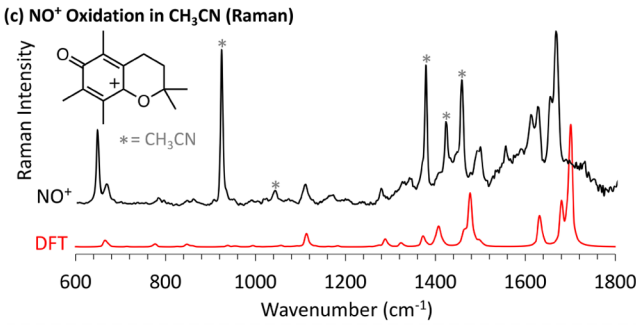
A weak signal at 466 nm can be detected in the PIDA oxidation, which we attribute to the phenoxenium PMHC-O<sup>+</sup>. The formation of both PMHC-O<sup>+</sup> and PMHC-O<sup>+</sup> during PIDA oxidation is consistent with a competitive dissociation mechanism in which both heterolysis and homolysis are detectable outcomes. A third intermediate detected at 630 nm is unknown but could likely be a reaction product of PMHC-O<sup>+</sup> like a charged or radical spiro-dimer.<sup>33</sup>

For completeness, we also report the UV-vis and EPR spectra of [PMHC-OH]<sup>•+</sup> (Figures S9 and S23). This radical cation was obtained using NO<sup>+</sup> in pure HFIP, which surprisingly blocked the formation of PMHC-O<sup>•</sup>. To reiterate, NO<sup>+</sup> oxidation of PHMC-OH did form the phenoxyl radical in a mixture of HFIP and CH<sub>3</sub>CN, but not in HFIP alone.

The reaction of **PIDA** with another phenol, 2,4,6-tri-<sup>t</sup>Buphenol, gave only the corresponding phenoxyl radical, which could be detected by UV—vis spectroscopy (see Figure S8). Without *p*-methoxy substituents like in **TMP-O**<sup>+</sup> and **PMHC-O**<sup>+</sup>, the phenoxenium of 2,4,6-tri-<sup>t</sup>Bu-phenol appears to be too unstable. Thus, it appears that free phenoxenium intermediates during PIDA oxidation are not generalizable phenomena. While we did observe and unambiguously characterize a free phenoxenium in the reaction of PIDA with **TMP-OH**, the







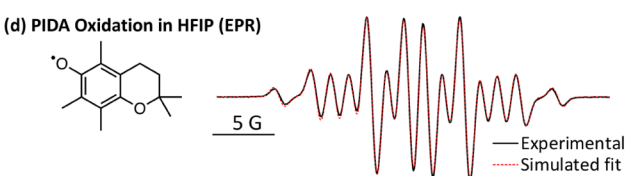


**Figure 6.** Identification of the intermediates seen during **PMHC-OH** oxidation. (a) Kinetic of the reaction between **PMHC-OH** (1.28 mM) and PIDA (1.28 mM) in HFIP at 10 °C. The kinetic trace is shown in the inset. (b) UV—vis spectra of **PMHC-OH** (10.0 mM) in CH<sub>3</sub>CN oxidized by electrochemistry (black line) and of **PMHC-OH** (4.28 mM) oxidized by excess NO+BF<sub>4</sub> (gray dotted line). (c) Raman signal of **PMHC-O**+ obtained by NO+SbF<sub>6</sub> oxidation in anhydrous CH<sub>3</sub>CN and comparison with DFT prediction. Obtained with B3LYP/Def2TZVP,SMD(HFIP) with pre-resonance effect. Peaks of the solvent are indicated with an asterisk. (d) X-band EPR signal of a solution of **PMHC-OH** (1.66 mM) and PIDA (1.67 mM) in HFIP and simulated fit for **PMHC-O**• in red.

reaction of PIDA with **PMHC-OH** or 2,4,6-tri-<sup>t</sup>Bu-butylphenol appears to predominantly give rise to phenoxyl radicals rather than free phenoxenium intermediates.

#### CONCLUSIONS

We report the first direct observation of a free phenoxenium intermediate in the reaction of phenols with hypervalent iodine reagents. Using a combination of UV–vis absorption, low-temperature resonance Raman spectroscopy, and DFT methods, we unambiguously detected the phenoxenium cation of TMP-OH during PIDA oxidation. TMP-O<sup>+</sup> has an absorption maximum at 510 nm ( $\varepsilon \approx 2.2 \times 10^3 \ \text{M}^{-1} \ \text{cm}^{-1}$ ) and is quite stable if minimal care is taken to avoid reactions

with water. Mechanistic investigations with DFT calculations suggest the mechanism of formation of TMP-O<sup>+</sup> occurs via heterolysis according to the classically proposed dissociative mechanism.

This is the first direct detection of a free phenoxenium cation in HVI dearomatization reactions, giving support to this ionic reaction pathway. However, we saw significantly more phenoxyl radical generation during the reaction of PIDA with less electron-rich phenols. The need for such an electron-rich phenol and strongly ionizing solvents to observe a phenoxenium intermediate may indicate that free phenoxenium species are not a generally observed pathway in these reactions. Direct detection of phenoxyl radicals during the PIDA oxidation of **PMHC-OH** and 2,4,6-tri-<sup>t</sup>Bu-phenol suggests that an alternative single electron transfer, proton-coupled electron transfer, or homolytic cleavage of the phenoxy-λ³-iodane complex mechanism will occur instead of the phenoxenium generation via heterolytic cleavage.

## **■ EXPERIMENTAL SECTION**

**Materials.** All materials were purchased from commercial sources and used without further purification. NO+SbF<sub>6</sub><sup>-</sup> was purchased from Sigma-Aldrich, NO+BF<sub>4</sub><sup>-</sup> from Oakwood Chemical, 2,4,6-trimethoxyphenol from AmBeed and Sigma-Aldrich, HFIP from Alfa Aesar, 2,2,5,7,8-pentamethyl-6-chromanol from Sigma-Aldrich, and anhydrous CH<sub>3</sub>CN from Sigma-Aldrich.

UV-Vis Kinetics of the Oxidation of TMP-OH by PIDA. The variable-temperature kinetics were acquired using an Agilent 8453 equipped with an RM6 Lauda Brinkmann refrigerated thermostatic bath. Short-neck sealable quartz cuvettes  $(1 \times 1 \text{ cm})$  were used for all experiments. The TMP-OH oxidation kinetic was obtained as follows. Stock solutions were prepared by dissolving PIDA (28.9 mg, 89.7 umol, 89.7 mM) in 1 mL of HFIP and TMP-OH (15.9 mg, 86.3 µmol, 86.3 mM) in 1 mL of HFIP. A cuvette containing 2 mL of HFIP was equilibrated at the desired temperature (10, 25, or 40  $^{\circ}$ C) and a blank spectrum was obtained. Using a syringe, 30 µL of the stock of PIDA was injected in the cuvette and a spectrum was recorded. A total of 30  $\mu$ L of the stock of TMP-OH was added, the cuvette was manually (and vigorously) shaken for a few seconds (<4 s) and the kinetic was started. The initial concentrations in TMP-OH and PIDA in the cuvette are 1.26 and 1.31 mM, respectively. We found that kinetics obtained with that method were reproducible. All kinetics were done on the same day from the same stock solutions (see Figure S1 for other temperatures). Over time, the initially clear solution turned purple, then bright red, and eventually became brown

UV-Vis Kinetics of the Oxidation of TMP-OH by NO+. Nitrosonium salts are not very soluble in HFIP; therefore, all of the NO+ oxidation results in HFIP are qualitative only. Stock solutions were prepared by dissolving NO<sup>+</sup>BF<sub>4</sub> $^-$  (8 mg, 68.5  $\mu$ mol, 68.5 mM) in 1 mL of HFIP, and TMP-OH (11.6 mg, 63.0  $\mu$ mol, 63.0 mM) in 1 mL of HFIP. Using a syringe, 40  $\mu$ L of each stock solution was added to 2 mL of HFIP in a quartz cuvette at 10 °C. The mixture instantaneously became yellow. Since the initial 8 mg did not fully dissolve, this solution contains less than 1 equiv in NO+ relative to TMP-OH, but the actual concentration is unknown. For the UV-vis with excess NO+BF<sub>4</sub>-, a quartz cuvette was directly loaded with  $\mathrm{NO^{+}BF_{4}}^{-}$  (19.8 mg, 169  $\mu$ mol, 89.0 mM) and 2 mL of HFIP. A stock of TMP-OH was added with a syringe, to reach a final concentration of 6.2 mM TMP-OH in the cuvette. This solution was heterogeneous due to undissolved NO+BF<sub>4</sub>- which accumulated at the bottom. The bottom part was deep red (due to the presence of TMP-O<sup>+</sup>) while the upper part was yellow-orange (due to the presence of TMP-O\*) (Figure S2). Upon vigorous shaking, the whole solution eventually became red, but this was too concentrated for our UV-vis measurement. Thus, a few drops of this solution were added to 2

mL of HFIP in another cuvette and the UV-vis was acquired at 10  $^{\circ}$ C. The final concentrations are unknown.

Low-Temperature Resonance Raman Spectroscopy for the Oxidation of TMP-OH by PIDA. The resonance Raman spectra of TMP-O+ were obtained from the reaction between PIDA and TMP-OH, at liquid nitrogen temperature to stabilize TMP-O+. This method was adapted from the one developed by Compton and Hammer. 18 It consists of taking a Raman spectrum of a frozen sample directly in liquid nitrogen, a technique they coined RUN (for Raman <u>Under liquid Nitrogen</u>). Starting reagents solutions were prepared by adding PIDA (29.6 mg, 91.9  $\mu mol,$  459 mM) in 0.2 mL of HFIP and **TMP-OH** (15.19 mg, 82.5  $\mu$ mol, 412 mM) in 0.2 mL of HFIP. The two solutions were mixed in a test tube, and it was rapidly submerged in liquid nitrogen (in less than 5 s from the mixing). Once cooled to liquid nitrogen temperature, the glass test tube was shattered, leaving the frozen reaction mixture as a solid pellet. This pellet was then transferred to a polystyrene foam box filled with liquid nitrogen. We found that lining the bottom of the polystyrene box with aluminum foil helped to reduce bubbling, which increased the signal due to a decrease in the turbulence at the liquid nitrogen's surface (see Figure S21 for a scheme of the setup). The use of a confocal Raman microscope (Renishaw inVia) allowed us to focus the laser on the frozen pellet, directly through the liquid nitrogen. The spectra were acquired with 532 nm excitation and 5% laser intensity (≈2.5 mW) with 1200 lines/mm and a 5× objective. Cosmic rays were removed by taking the median intensity at each frequency for more than three acquisitions. The spectra were baseline-corrected with the WiRE 5.1 software.

The Raman spectra of **PMHC-O**<sup>+</sup> were obtained using a similar procedure but from a solution of **PMHC-OH** (101.58 mg, 461  $\mu$ mol, 0.154 M) in 3 mL of anhydrous CH<sub>3</sub>CN. This solution was first cooled at -45 °C in a dry ice bath, and then an excess of NO<sup>+</sup>SbF<sub>6</sub><sup>-</sup> (277.10 mg, 1.04 mmol, 0.347 M) was added. The mixture became bright orange, and it was then submerged in liquid nitrogen for the low-temperature Raman measurements.

Resonance Raman Spectroscopy for the Oxidation of TMP-OH by NO<sup>+</sup> in CH<sub>3</sub>CN. When using NO<sup>+</sup>SbF<sub>6</sub><sup>-</sup> and CH<sub>3</sub>CN, the signal at 510 nm corresponding to the phenoxenium cation TMP-O+ decayed slowly enough to work at room temperature (Figure S5b for the UV-vis spectra). This simplified the Raman acquisition as it did not require quenching or low temperatures. A short-neck quartz cuvette was loaded with NO<sup>+</sup>SbF<sub>6</sub><sup>-</sup> (15.48 mg,  $5.82 \times 10^{-5}$  mol) and 2 mL of anhydrous CH3CN was injected. Using a stock solution, TMP-OH was also injected to reach a final concentration of 6.8 mM in the cuvette. The solution immediately turned bright red. Raman acquisition was done by placing the cuvette at a  ${\sim}45^{\circ}$  angle and the laser was focused through the quartz cuvette (the experimental setup is presented in Figure S20). A 5× objective was used with a 532 nm laser. Some signal from the solvent (CH<sub>3</sub>CN) and products remained despite the good amplification conditions. Thus, 10  $\mu$ L of water was injected into the cuvette and the solution immediately turned yellow due to the transformation of TMP-O+ into 2,4-dimethoxybenzoquinone (Figure S10 for a photograph of the cuvette and Figure S11 for the UV-vis spectra). Raman spectra of the yellow mixture, pure CH<sub>3</sub>CH, and the quartz cuvette were obtained in the same condition and subtracted from the original spectrum to isolate the signal of TMP-O<sup>+</sup> (Figure S14). GC-MS of the resulting yellow mixture was used to identify the presence of 2,4-dimethoxybenzoquinone (Figure

**Spectroelectrochemistry.** UV–vis spectra of the electrochemical oxidation products (Figure 1c) were obtained with a honeycomb cell kit by Pine Research equipped with a gold working and counter electrode. The reference electrode was Ag/Ag<sup>+</sup>, and the electrolyte was 0.2 M tetraethylammonium tetrafluoroborate. The spectra were acquired with an Agilent Cary 60 UV–vis spectrometer and a Princeton Applied Research 263A potentiometer. The quartz cuvette was filled with a solution of TMP-OH (18.13 mg, 98.4  $\mu$ mol, 9.84 mM) in HFIP containing the electrolyte. Cyclic voltammograms (CVs) were obtained with a 100 mV s<sup>-1</sup> scan rate. A fresh solution was used for the UV–vis spectroscopy and the CVs. The UV–vis

spectra at different potentials were obtained by (1) applying a constant potential for 15 s, (2) taking a UV–vis spectra, and then repeating with increments of potentials. The solution was degassed with  $N_2$  before the measurements and kept under a continuous flow of  $N_2$  for the duration of the experiment. The CVs and UV–vis are shown in Figure S22.

Electron Paramagnetic Resonance (EPR) Spectroscopy. EPR spectra were recorded with an X-band EPR (Bruker AV III 600) operating at 9.44 GHz. The temperature was set to 283 K (10  $^{\circ}$ C) for all experiments. The following parameters were used: module frequency = 100 kHz, module amplitude = 0.5 G, receiver gain = 30 dB, time constant = 0.01 ms, sweep time of 20.97 s, and number of scans = 3. A capillary quartz tube was used due to the high dielectric constant of HFIP. The stock solutions were pre-degassed and precooled in an ice bath before the experiment. For both the EPR spectra shown in Figure 3, the reaction mixture was prepared by mixing equal amounts of the stock solutions of the oxidizing agent (PIDA or NO+) and of TMP-OH. This corresponds to "time zero". Using a gas-tight syringe, the reaction mixture was then injected into a degassed EPR tube and placed in the resonator. Tuning the instrument required a few minutes each time; therefore, the beginning of the kinetics is missing a few data points. The area under the curve for each spectrum was obtained from double integration of the EPR signal. The g-values were calibrated using a standard of (2,2,6,6tetramethylpiperidin-1-yl)oxyl (TEMPO) in MeOH, which has a known g-value of 2.0061.3

For PIDA oxidation (Figure 3b), 20  $\mu$ L of a stock of PIDA (27.9 mg,  $8.66 \times 10^{-5}$  mol, 86.6 mM) was injected into a test tube containing 1 mL of HFIP. The reaction was initiated by adding 20  $\mu$ L of a stock of **TMP-OH** (15.2 mg,  $8.63 \times 10^{-5}$  mol, 86.3 mM) in the test tube. The mixture was then transferred to the quartz capillary. The final concentration is 1.66 mM **TMP-OH** and 1.67 mM PIDA.

For NO $^+$  oxidation (Figure 3a), 500  $\mu$ L of a stock solution of TMP-OH in 1 mL of HFIP (12.0 mg, 6.51  $\times$  10 $^{-5}$  mol, 32.6 mM) was mixed with an equal volume (500  $\mu$ L) of a stock solution of NO $^+$ BF $_4^-$  in 1 mL of HFIP (11.6 mg, 9.93  $\times$  10 $^{-5}$  mol, 33.10 mM). The mixture was then transferred to the quartz capillary. The final concentration was 16.3 mM TMP-OH and 16.6 mM NO $^+$ .

Hyperfine coupling constants were calculated with Gaussian 16<sup>35</sup> at the B3LYP/EPR-III//B3LYP/Def2TZVP,SMD(HFIP) level of theory. The MATLAB R2018a software and the free EasySpin toolbox (www.easyspin.org) were used to simulate EPR spectra from the DFT-predicted hyperfine coupling constants. The garlic module was used, which is designed for isotropic and fast-motion signal in solution. Only hydrogens were used to simulate the spectra of the organic radicals. For the simulated fit, the same nuclei system was used, but the hyperfine coupling constants were allowed to fluctuate to reduce the difference between the fit and the experimental spectra. The spin systems are presented in Tables S2–S5.

Titration Experiments. Starting from the hypothesis that the peaks at 400 and 690 nm originated from the reaction between TMP-OH and TMP-O+ to form the dimer BP-O+, we performed two titration experiments. PIFA is strongly oxidizing and led to (almost) exclusively the phenoxenium TMP-O+ when oxidizing TMP-OH in HFIP (EPR shows a weak signal assigned to the dimer byproduct, but UV-vis spectroscopy indicates its concentration is much smaller than when using PIDA). Therefore, titration of TMP-OH in an excess of PIFA should first rapidly oxidize TMP-OH into TMP-O+ with little to no possibility of reacting with other TMP-OH, since most of it is already oxidized. Indeed, the titration experiment shown in Figure S6 shows that phenoxenium is directly formed. As PIFA gets consumed during the titration, the titrated TMP-OH is no longer oxidized, which leads to a mixture of TMP-OH and TMP-O+. The two compounds should therefore be able to react together when the ratio of TMP-OH/PIFA reaches a value close to unity. At this point, the peaks at 400 and 690 nm were indeed observed. Another titration experiment was performed, this time by the addition of PIFA in an excess of TMP-OH (Figure S7). This experiment showed the 400 nm signal is formed at the start of the titration. It is not clear however why

the dimer, BP-O\*, stops being formed at a ratio of PIFA/TMP-OH much lower than unity.

The slope for the initial data points during the titration of TMP-OH in PIFA (Figure S6, linear region) was used to get an approximation of the extinction coefficient of TMP-O<sup>+</sup>. Assuming 1 equiv of PIFA leads to 1 equiv of TMP-O<sup>+</sup> and that TMP-O<sup>+</sup> is stable, its extinction coefficient at 510 nm was found to be  $\varepsilon_{510\,\mathrm{nm}} = 2207\,\mathrm{mol}^{-1}\,\mathrm{cm}^{-1}$ , reported as  $2.2\times10^3\,\mathrm{M}^{-1}\,\mathrm{cm}^{-1}$  in the manuscript.

**Calculations.** All calculations were performed using the Gaussian16 suite, <sup>35</sup> at the exception of the minimum energy crossing point (MECP) and STEOM-DLPNO-CCSD calculations which were performed with Orca 4.2.<sup>36</sup>

Pre-resonance Raman spectra were obtained from the following method. Optimization and frequency calculations were done at the B3LYP/6-311+G(2d,2p),SMD(HFIP) level of theory using Gaussian16. A TD-DFT calculation was done at the same level of theory on the optimized structure to get the predicted absorption spectra. The excitation wavelength used to simulate the pre-resonance Raman spectra was selected according to the experimental UV-vis and experimental excitation of 532 nm. For example, Figure S15 shows that a 532 nm excitation is approximately 20 nm red-shifted from the absorption maximum of TMP-O+ at 510 nm. Gaussian's manual indicates that the pre-resonance Raman spectrum should use the same redshift (20 nm). However, from our experience, best fit with experimental values may be more or less red-shifted depending on the peak's width. After modeling the Raman spectra with excitation at multiple wavelengths between 550 and 700 nm, we found that simulating an excitation at 630 nm led to the best correlation with experiment in terms of peak intensities (see Figure S17 for the comparison between predicted and experimental Raman intensities).

The predicted absorption spectra for BP-O $^{\bullet}$  and TMP-O $^{+}$  (shown in Figure 1d) were obtained with TD-DFT at the B3LYP/Def2TZVP,SMD(HFIP) level of theory for n=12 states. In addition, higher-level STEOM-DLPNO-CCSD/Def2TZVP,CPCM(CH<sub>3</sub>CN) calculations were used to get the predicted UV-vis spectra for TMP-O $^{+}$  (Figure SSa). This method performed better than TD-DFT, but is unfortunately only available for closed-shell molecules in Orca 4.2 so it could not be used for the radical BP-O $^{\bullet}$ .

The energy profile of the reaction (Figure 5) was plotted from DFT calculations performed at the M06-2X/Def2TZVP,SMD(HFIP) level of theory. Others have also used this functional for hypervalent iodine compound, including PIDA, prior to our study. We could not locate some of the transition states when using the B3LYP functional, so M06-2X was used.

Minimum energy crossing point (MECP) calculations are not available in Gaussian16, so Orca 4.2 was used. The SurfCrossOpt and SurfCrossNumFreq keywords were used to calculate the MECP between the first singlet and first triplet. These calculations were done at the M06-2X/Def2TZVP,SMD(CH<sub>3</sub>CN) level of theory. Analysis of the orbital for the MECP structure in its triplet configuration confirmed that the two radicals are indeed disjoint: one is on the 2,4,6-trimethoxyphenoxyl moiety and the other is on the iodine (Figure S25). The starting iodane complex (compound 11, (MeO)<sub>3</sub>-phenoxy-λ<sub>3</sub>-iodane) was also calculated with Orca to get the energy difference from that step since other energies were obtained with Gaussian.

Custom solvent specifications for HFIP were obtained from Richmond et al.  $^{37}$  and are given in Section S7 in the Supporting Information.

## ASSOCIATED CONTENT

## Supporting Information

The Supporting Information is available free of charge at https://pubs.acs.org/doi/10.1021/acs.joc.2c01765.

Variable-temperature UV-vis experiments, quenching experiments, low-temperature Raman experiments, GC-MS, hyperfine coupling constants, and calculated geometries (PDF)

#### AUTHOR INFORMATION

#### **Corresponding Author**

Mathieu Frenette — Department of Chemistry, Quebec Centre for Advanced Materials and NanoQAM, Université du Québec à Montréal, Montréal, Québec H3C 3P8, Canada; orcid.org/0000-0003-0491-6879; Email: frenette.mathieu@uqam.ca

#### **Authors**

Antoine Juneau — Department of Chemistry, Quebec Centre for Advanced Materials and NanoQAM, Université du Québec à Montréal, Montréal, Québec H3C 3P8, Canada Iannick Lepage — Department of Chemistry, Quebec Centre for Advanced Materials and NanoQAM, Université du Québec à Montréal, Montréal, Québec H3C 3P8, Canada Sami G. Sabbah — Department of Chemistry, Quebec Centre for Advanced Materials and NanoQAM, Université du Québec à Montréal, Montréal, Québec H3C 3P8, Canada Arthur H. Winter — Department of Chemistry, Iowa State University, Ames, Iowa 50010, United States; orcid.org/0000-0003-2421-5578

Complete contact information is available at: https://pubs.acs.org/10.1021/acs.joc.2c01765

#### **Author Contributions**

The original idea was developed by A.J. and M.F. The EPR, UV-vis, resonance Raman, and spectroelectrochemistry experiments, as well as DFT calculations were designed and performed by A.J., under the supervision of M.F. and A.H.W. The co-author I.L. performed CVs, UV-vis, and controls with PIFA. The co-author S.G.S. performed DFT calculations on PIDA and participated in the experimental design. The manuscript was written by A.J. and edited by M.F. and A.H.W. All authors participated in discussing the results and approved the manuscript.

## Notes

The authors declare no competing financial interest.

#### ACKNOWLEDGMENTS

The authors gratefully acknowledge NSERC for funding in the form of a Discovery Grant to M.F. (RGPIN-2016-06773) and an Alexander Graham Bell graduate scholarship to A.J. A.H.W. thanks the NSF for support (NSF CHE 2055335 and CHE 1764235). The authors are also grateful to NanoQAM for Raman access, to Compute Canada and Gaussian for computational resources, and to Iowa State University for EPR access. They also thank Prof. Sylvain Canesi and Dr. Elsa Deruer for their helpful insights into hypervalent iodine chemistry, and Dr. Sarah Cady from Iowa State University for sharing her expertise in EPR spectroscopy.

## REFERENCES

- (1) Zhang, B.; Li, X.; Guo, B.; Du, Y. Hypervalent iodine reagents-mediated reactions involving rearrangement process. *Chem. Commun.* **2020**, *56*, 14119–14136.
- (2) Deruer, E.; Coulibali, S.; Boukercha, S.; Canesi, S. Carbon-phosphorus bond formation on anilines mediated by a hypervalent iodine reagent. *J. Org. Chem.* **2017**, *82*, 11884–11890.
- (3) Dohi, T.; Ito, M.; Yamaoka, N.; Morimoto, K.; Fujioka, H.; Kita, Y. Hypervalent iodine (III): Selective and efficient single-electron-transfer (SET) oxidizing agent. *Tetrahedron* **2009**, *65*, 10797–10815. (4) Dohi, T.; Maruyama, A.; Takenaga, N.; Senami, K.; Minamitsuji, Y.; Fujioka, H.; Caemmerer, S. B.; Kita, Y. A chiral hypervalent iodine

- (III) reagent for enantioselective dearomatization of phenols. *Angew. Chem., Int. Ed.* **2008**, 47, 3787–3790.
- (5) Tang, T.; Harned, A. M. Experimental evidence for the formation of cationic intermediates during iodine (III)-mediated oxidative dearomatization of phenols. *Org. Biomol. Chem.* **2018**, *16*, 8249–8252.
- (6) Harned, A. M. Concerning the mechanism of iodine (iii)-mediated oxidative dearomatization of phenols. *Org. Biomol. Chem.* **2018**, *16*, 2324–2329.
- (7) Kraszewski, K.; Tomczyk, I.; Drabinska, A.; Bienkowski, K.; Solarska, R.; Kalek, M. Mechanism of iodine (III)-promoted oxidative dearomatizing hydroxylation of phenols: Evidence for a radical-chain pathway. *Chem. Eur. J.* **2020**, *26*, 11584–11592.
- (8) Ganji, B.; Ariafard, A. DFT mechanistic investigation into phenol dearomatization mediated by an iodine (iii) reagent. *Org. Biomol. Chem.*, **2019**, *17*, 3521–3528.
- (9) Wang, X.; Studer, A. Iodine (III) reagents in radical chemistry. Acc. Chem. Res. 2017, 50, 1712–1724.
- (10) Hyatt, I. F. D.; Dave, L.; David, N.; Kaur, K.; Medard, M.; Mowdawalla, C. Hypervalent iodine reactions utilized in carbon-carbon bond formations. *Org. Biomol. Chem.* **2019**, *17*, 7822–7848.
- (11) Colomer, I.; Batchelor-McAuley, C.; Odell, B.; Donohoe, T. J.; Compton, R. G. Hydrogen bonding to hexafluoroisopropanol controls the oxidative strength of hypervalent iodine reagents. *J. Am. Chem. Soc.* **2016**, *138*, 8855–8861.
- (12) Williams, L. L.; Webster, R. D. Electrochemically controlled chemically reversible transformation of  $\alpha$ -tocopherol (vitamin E) into its phenoxonium cation. *J. Am. Chem. Soc.* **2004**, *126*, 12441–12450.
- (13) Gagnepain, J.; Méreau, R.; Dejugnac, D.; Léger, J.-M.; Castet, F.; Deffieux, D.; Pouységu, L.; Quideau, S. Regio-and stereoselectivities in Diels—Alder cyclodimerizations of orthoquinonoid cyclohexa-2, 4-dienones. *Tetrahedron* **2007**, *63*, 6493–6505.
- (14) Quideau, S.; Pouységu, L.; Avellan, A.-V.; Whelligan, D. K.; Looney, M. A. Hypervalent iodine (III)-mediated oxidative acetoxylation of 2-methoxyphenols for regiocontrolled nitrogen benzannulation. *Tetrahedron Lett.* **2001**, 42, 7393–7396.
- (15) Kürti, L.; Szilágyi, L.; Antus, S.; Nógrádi, M. Oxidation of omethoxyphenols with a hypervalent iodine reagent: Improved synthesis of asatone and demethoxyasatone. *Eur. J. Org. Chem.* **1999**, *10*, 2579–2581.
- (16) Iwado, A.; Mifune, M.; Kato, J.; Oda, J.; Chikuma, M.; Motohashi, N.; Saito, Y. Catalytic activity of anion-exchange resins modified with metal-porphine in oxidative reactions of phenols. *Chem. Pharm. Bull.* **2000**, *48*, 1831–1832.
- (17) Li, M. D.; Hanway, P. J.; Albright, T. R.; Winter, A. H.; Phillips, D. L. Direct spectroscopic observation of closed-shell singlet, open-shell singlet, and triplet p-biphenylyloxenium ion. *J. Am. Chem. Soc.* **2014**, *136*, 12364–12370.
- (18) Compton, R. N.; Hammer, N. I. Raman under liquid nitrogen (RUN). J. Phys. Conf. Ser. 2014, 548, No. 012017.
- (19) Kita, Y.; Dohi, T.; Nakae, T.; Takenaga, N.; Uchiyama, T.; Fukushima, K.-i.; Fujioka, H.  $\mu$ -Oxo-bridged hypervalent iodine (III) compound as an extreme oxidant for aqueous oxidations. *Synthesis* **2012**, *44*, 1183–1189.
- (20) Stoll, S.; Schweiger, A. EasySpin, a comprehensive software package for spectral simulation and analysis in EPR. *J. Magn. Reson.* **2006**, *178*, 42–55.
- (21) Lucarini, M.; Pedrielli, P.; Pedulli, G. F.; Cabiddu, S.; Fattuoni, C. Bond dissociation energies of O–H bonds in substituted phenols from equilibration studies. *J. Org. Chem.* **1996**, *61*, 9259–9263.
- (22) Kita, Y.; Tohma, H.; Hatanaka, K.; Takada, T.; Fujita, S.; Mitoh, S.; Sakurai, H.; Oka, S. Hypervalent iodine-induced nucleophilic substitution of para-substituted phenol ethers. Generation of cation radicals as reactive intermediates. *J. Am. Chem. Soc.* 1994, 116, 3684–3691.
- (23) Kita, Y.; Takada, T.; Tohma, H. Hypervalent iodine reagents in organic synthesis: Nucleophilic substitution of p-substituted phenol ethers. *Pure Appl. Chem.* **1996**, *68*, *627*–*630*.

- (24) Hussein, A. A.; Ma, Y.; Al-Yasari, A. Hypervalent iodine-mediated styrene hetero- and homodimerization initiation proceeds with two-electron reductive cleavage. *Eur. J. Org. Chem.* **2020**, 2020, 7219–7228.
- (25) Miranda, M. A.; Izquierdo, M. A. Chemical and transient spectroscopic evidence for C2–C3 cleavage of 2,3-diaryloxetane radical cations. *Chem. Commun.* **2003**, *3*, 364–365.
- (26) Hyun, S.-M.; Yuan, M.; Maity, A.; Gutierrez, O.; Powers, D. C. The role of iodanyl radicals as critical chain carriers in aerobic hypervalent iodine chemistry. *Chem* **2019**, *5*, 2388–2404.
- (27) Ramos-Villaseñor, J. M.; Rodríguez-Cárdenas, E.; Barrera Díaz, C. E.; Frontana-Uribe, B. A. Use of 1,1,1,3,3,3-hexafluoro-2-propanol (HFIP) co-solvent mixtures in organic electrosynthesis. *J. Electrochem. Soc.* **2020**, *167*, No. 155509.
- (28) Guérard, K. C.; Chapelle, C.; Giroux, M.-A.; Sabot, C.; Beaulieu, M.-A.; Achache, N.; Canesi, S. An unprecedented oxidative Wagner–Meerwein transposition. *Org. Lett.* **2009**, *11*, 4756–4759.
- (29) Yusubov, M. S.; Zhdankin, V. V. Zefirov's reagent and related hypervalent iodine triflates. *Mendeleev Commun.* **2021**, *31*, 282–287.
- (30) Bowry, V. W.; Ingold, K. U. Extraordinary kinetic behavior of the alpha-tocopheroxyl (vitamin E) radical. *J. Org. Chem.* **1995**, *60*, 5456–5467.
- (31) Lee, S. B.; Lin, C. Y.; Gill, P. M.; Webster, R. D. Transformation of  $\alpha$ -tocopherol (vitamin E) and related chromanol model compounds into their phenoxonium ions by chemical oxidation with the nitrosonium cation. *J. Org. Chem.* **2005**, 70, 10466–10473.
- (32) Chen, S.; Peng, H. M.; Webster, R. D. Infrared and UV—vis spectra of phenoxonium cations produced during the oxidation of phenols with structures similar to vitamin E. *Electrochim. Acta* **2010**, *55*, 8863–8869.
- (33) Chauhan, M.; Dean, F. M.; Hindley, K.; Robinson, M. The phenoxylium ion from  $\alpha$ -tocopherol spirodimer and its significance for the mechanism of oxidative coupling in phenols. *J. Chem. Soc. D* **1971**, *0*, 1141–1143.
- (34) Herb, K.; Tschaggelar, R.; Denninger, G.; Jeschke, G. Double resonance calibration of g factor standards: Carbon fibers as a high precision standard. *J. Magn. Reson.* **2018**, 289, 100–106.
- (35) Frisch, M. J.; Trucks, G. W.; Schlegel, H. B.; Scuseria, G. E.; Robb, M. A.; Cheeseman, J. R.; Montgomery, J. A., Jr.; Vreven, T.; Kudin, K. N.; Burant, J. C.; Millam, J. M.; Iyengar, S. S.; et al. *Gaussian 16*, revision A.03; Gaussian, Inc.: Wallingford, CT, 2016.
- (36) Neese, F. The ORCA program system. Wiley Interdiscip. Rev.: Comput. Mol. Sci. 2012, 2, 73–78.
- (37) Richmond, E.; Yi, J.; Vukovic, V. D.; Sajadi, F.; Rowley, C. N.; Moran. *J. Chem. Sci.* **2018**, *9*, 6411–6416.